Highly Stretchable Two-Dimensional Auxetic Metamaterial Sheets Fabricated *via* Direct-Laser Cutting

Luke Mizzi, Enrico Salvati, Andrea Spaggiari, Jin-Chong Tan, Alexander M. Korsunsky

Supplementary Information

1. Material Properties of Black Rubber

The tensile stress-strain plot of the black rubber base material used to produce the perforated architectures was found by stretching a standard planar dog-bone with a gauge length of 5 cm. A 5-Parameter Mooney-Rivlin Hyperelastic model was then fitted over the stress-strain data up to a strain of 55% and used to run the non-linear FE simulations. The following parameters were used to describe the curve fit:

Parameter	Value (Pa)
C01	-462915
C02	-5314541
C10	1885146
C11	6306033
C20	-1567704
D1	0

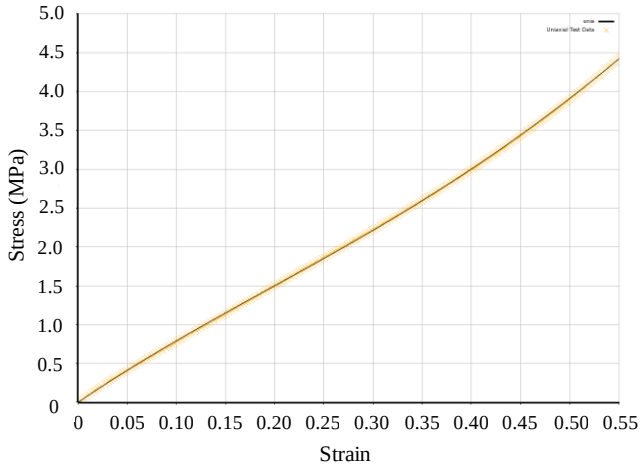

Figure S1: Stress-strain plot showing the experimental data and curve fitting of the black rubber used.

2. Digital Image Correlation (DIC) measurements

The experimental samples were uniaxially stretched at a rate of 1.5 mm/s using a DEBEN® Microtensile loading device with a 20 N loadcell. A Point Grey FlyCap® camera was used to capture a series of high-resolution images of the deformation over time which were then used to conduct the DIC measurements using Matlab. As shown in Figure S2, where Architecture I is presented, the experimental Poisson's ratio was measured from two distinct regions: a) from the central region marked in yellow and b) that of the entire system marked in red. In the first case, as shown in Figure S2b, eight points were chosen for tracking, with two placed on each edge of the central repeating unit of the architecture. In order to determine the average strain in the *y*-direction the following equation was used:

$$\bar{\varepsilon}_y = \frac{1}{2}\left(\frac{(Y1_i - Y3_i) - (Y1_0 - Y3_0)}{Y1_0 - Y3_0} + \frac{(Y2_i - Y4_i) - (Y2_0 - Y4_0)}{Y2_0 - Y4_0} \right)$$

where Yj_0 represents the *y*-coordinate of the point in the first reference image and Yj_i represents the *y*-coordinate of the same point in the subsequent images. The same reasoning was used to find the average strain in the *x*-direction, using the *x*-coordinates of the other four points:

$$\bar{\varepsilon}_x = \frac{1}{2}\left(\frac{(X5_i - X7_i) - (X5_0 - X7_0)}{X5_0 - X7_0} + \frac{(X6_i - X8_i) - (X6_0 - X8_0)}{X6_0 - X8_0} \right)$$

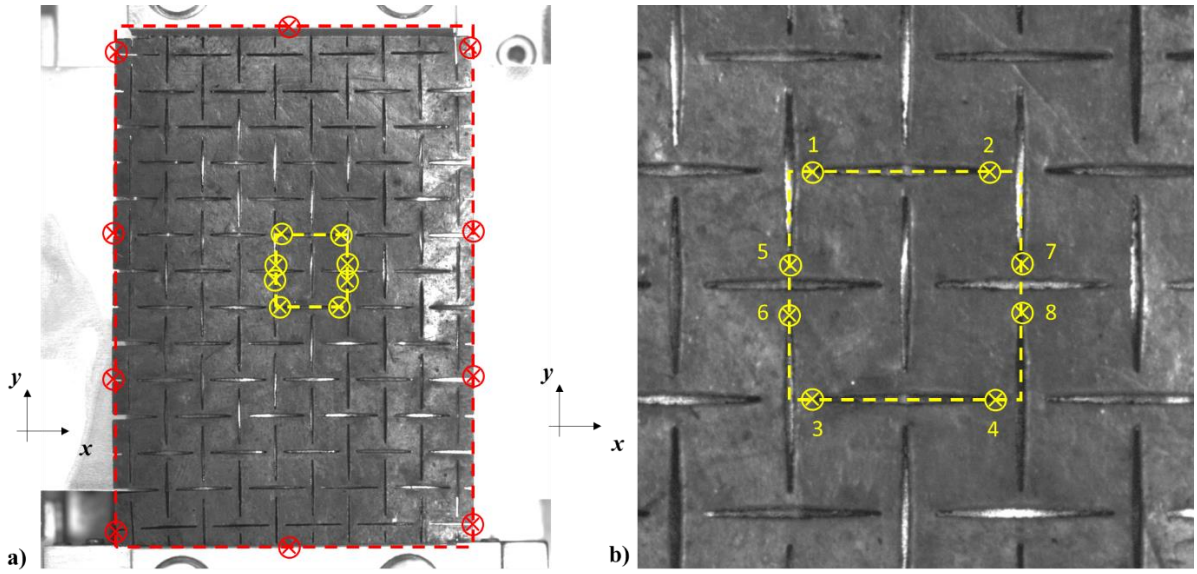

Figure S2: Diagrams showing how the markers were placed for the DIC measurements.

The Poisson's ratio of the central region was then calculated from these strains. The same technique was used to measure the Poisson's ratio of the whole system, except that in this case the strains in the *y*-direction were measured from two points only since the upper part of the system is clamped by the microtensile loader and thus the strain in the *y*-direction is

uniform throughout. On the other hand, the system is not constrained from the *x*-direction and thus four sets of points are used to measure the average strain in the *x*-direction; two sets near the centre and another pair of sets at both edges. The same measurement method was used for the FE simulations on the equivalent finite systems, with readings taken from both the central repeating unit and the entire overall system.

3. 2D Finite Element Simulations

Finite Element Simulations were conducted on infinite and finite systems of each of the twelve geometries investigated in this study. Both sets of simulations were conducted under plane-stress conditions using the PLANE183 element and using the hyperelastic model presented in Section 1 as the base material property.

In the case of the infinite systems, a single repeating unit cell was simulated using periodic boundary conditions. Constraint equations were applied on the boundary nodes of the system in order to ensure that the deformation on each edge corresponds to its opposing counterpart and the system was aligned along the *y*-axis by fixing one node in the bottom edge preventing it from undergoing displacement in the *x*- and *y*-directions and the corresponding node in the top edge was fixed from the *x*-direction only in order to prevent rigid body rotation. Deformation was induced through the application of a tensile force in the *y*-direction on the upper and lower edges of the system. This technique for implementation of periodic boundary conditions has been validated and used to study other perforated architectures in [16, 28, 29, 51].

For the finite systems, 2D equivalents of the experimental prototypes were modelled and loaded. Therefore, these systems contained multiple repeating units and were simulated under experimental loading conditions. This entailed fixing the lower edge in the *x*- and *y*-directions and fixing the upper edge nodes in the *x*-direction and applying a fixed displacement in the y-direction. The right and left edges of the system were left free and unconstrained.

4. 3D Simulation of Architecture IX

In order to analyze the out-of-plane deformation of Architecture IX an additional 3D simulation with enforced periodicity in the *xy*-plane was conducted. The 3D system was meshed using tetrahedral 8-node SOLID187 elements. Roller displacement constraints blocking displacement in the *x*-direction were placed along the entire left edge of the system (see Figure S3) while the nodes on the opposing edge were coupled and constrained to remain aligned with the *y*-axis at all times. The system was fixed in the *z*- and *y*-directions only from the nodes at the midpoint of the thickness (*z*-length) of the system from the bottom edge as shown in Figure S3. An enforced displacement in the *y*-direction was applied at the opposing midpoint edge at the top of the geometry along with a fix on movement in the *z*-direction. This ensures that the two edges marked with crosses in Figure S3 remain fixed in the *z*-direction, and hence aligned with the *y*-axis, at all times whilst the rest of the system may deform freely in the *z*-direction. In addition to all this, since the deformation observed on the experimental sample was axially asymmetric, a small force was applied on the surface of the central re-entrant region of the system in the *z*-direction in order to kickstart and direct the asymmetric out-of-plane deformation of the architecture.

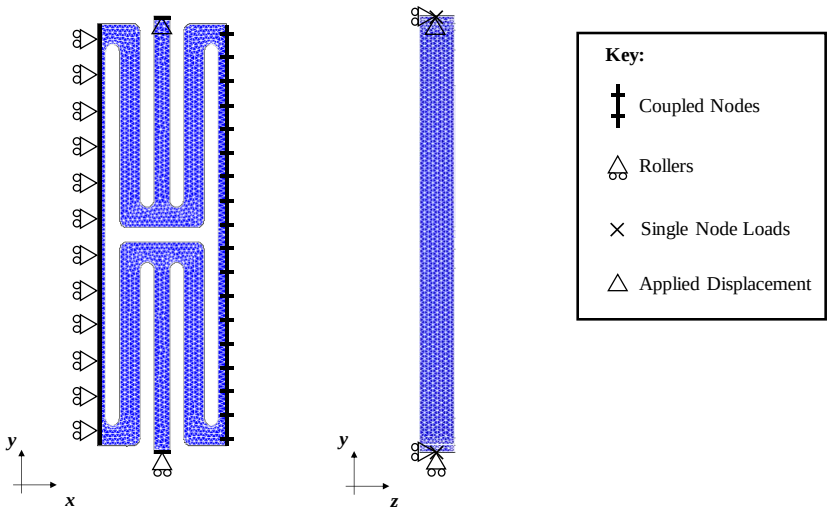

Figure S3: Diagram showing the fixes, coupling and loads applied to the 3D system.

5. Force-displacement plots of Experimental Samples

The force-displacement plots for the twelve laser-cut architectures were obtained using a DEBEN microtensile loading device with a 20N load cell. This microtensile loading device has a maximum travel distance of 10 mm and was set to a travel speed of 1.5 mm/minute. Set 1 architectures (I-III) were significantly stiffer than the other geometries while Architectures V and VI were the least stiff. In addition, the trends for the force-displacement plots of Architectures VI-IX and XII mirror those observed for the corresponding periodic simulations shown in Figure S4.

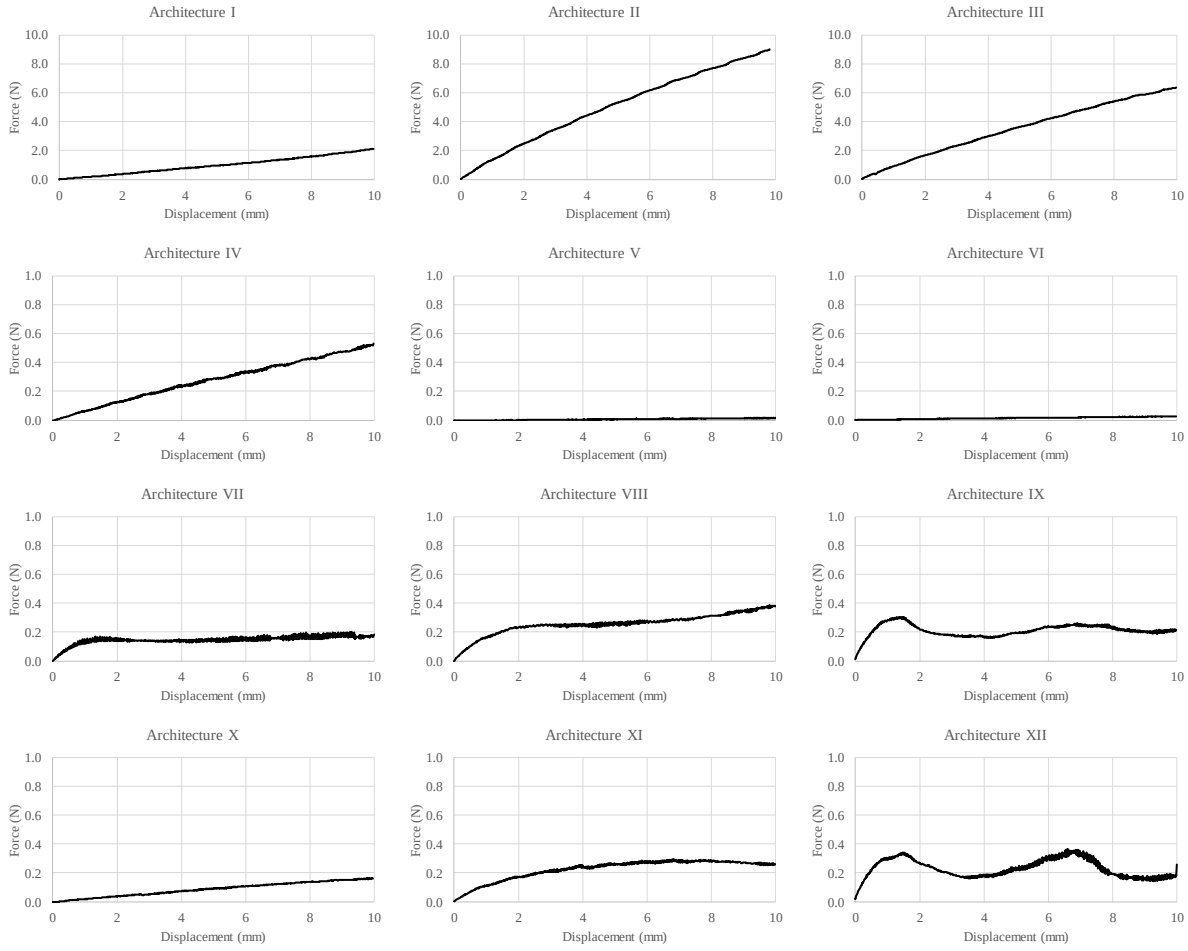

Figure S4: Force-displacement plots obtained from the experimental loading of the twelve architectures (full dimensions are provided in Table 1 in the main manuscript).

6. Stress-Strain plots of Periodic Systems

The stress-strain plots for the twelve architectures obtained from the plane-stress simulations on single unit cells with periodic boundary conditions are presented below. As one may observe from Figure S5, the plots have two distinct profiles. In Architectures I-VI, X and XI, the stress-strain plot is either linear or the Young's modulus progressively increases upon increasing strain, leading to a distributed deformation gradient in a finite system. On the other hand, Architectures VII-IX and XII show a decrease in the Young's modulus upon increasing strain which leads to the deformation being concentrated along distinct pathways or veins within the finite simulations and experimental systems.

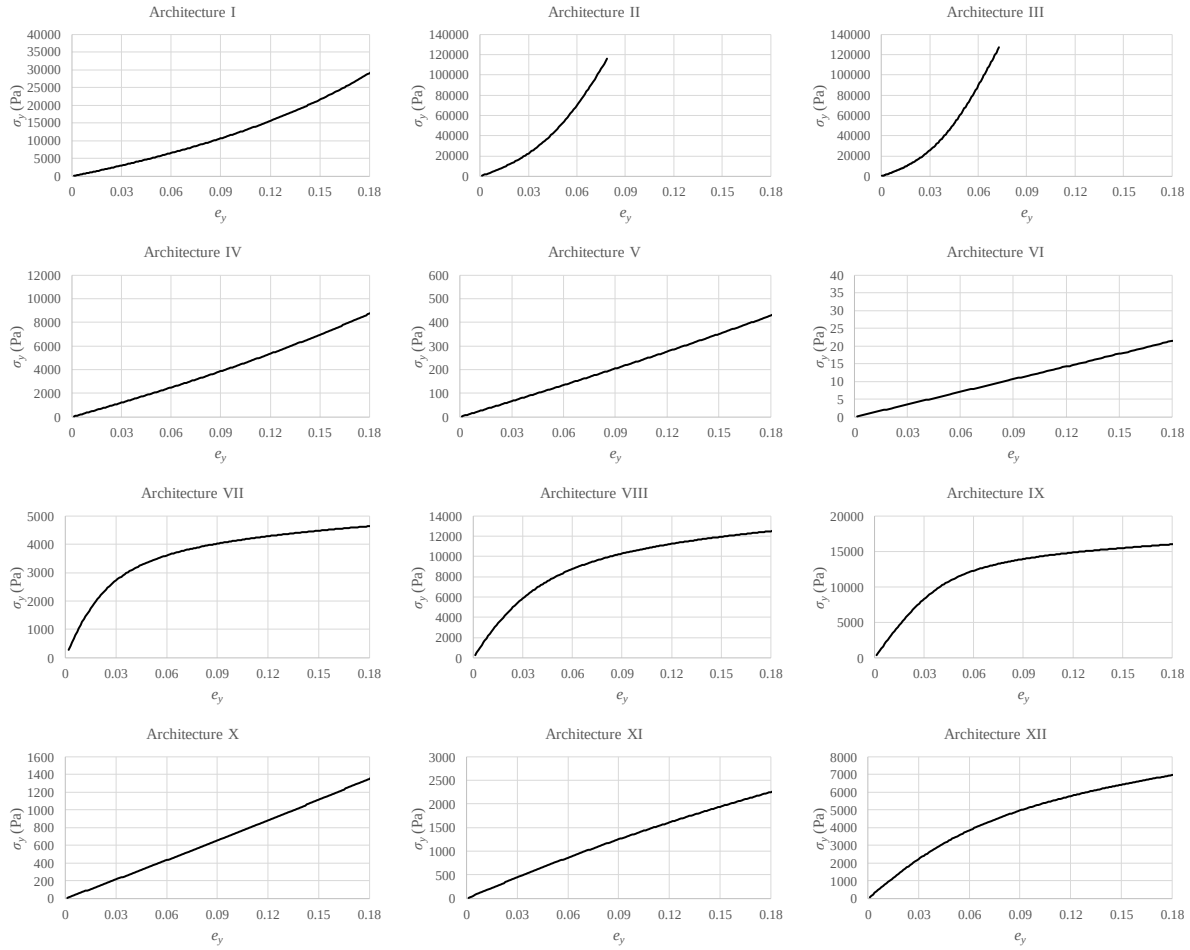

Figure S5: Stress-strain plots obtained from planar periodic simulations on each of the twelve architectures.